ADVANCED FUNCTIONAL MATERIALS
www.afm-journal.de

# All-in-One Soft Capacitive Pressure Sensor with Adaptive Self-Healing Property in Diverse Harsh Environments

*Jiaxin Guo, Lingyu Zhao,* Zengbai Ouyang, Qiong Zuo, Yongzhi Liang, and Jinsong Leng**

**High-performance soft capacitive pressure sensors have attracted attention due to their wide application in health monitoring, human–machine interaction and intelligent robotics. However, their deployment in diverse environments often subjects them to mechanical damage, rendering them unable to provide reliable signals during long-term use. Herein, an all-in-one capacitive pressure sensor is designed with a full-module self-healing function based on chemically modified polydimethylsiloxane (PDMS). Dynamic imine and disulfide bonds incorporated into the polymer network enable efficient autonomous healing of the polymer under ambient conditions, aqueous settings, at subzero temperatures (−15 °C), and in high-concentration saline environments (35 wt% NaCl). The electrode and dielectric layer are fabricated by using multi-walled carbon nanotubes (CNT) and PEDOT:PSS as the fillers. Traditional self-healable capacitive pressure sensors usually focus on endowing the healability of individual components, while the mechanical mismatch between different components hinders the entire device from self-healing. The all-in-one sensor design can avoid the mechanical mismatch and delamination between components, thus rendering a self-healing property at the device level. When integrated into a soft robotic gripper and submarine model, the sensor consistently restored sensing properties after damage. These results confirm its significant promise for application as a robust, self-healing sensor across a wide range of environments.**

## 1. Introduction

In recent years, the rapid development of soft robotics[1] and wearable devices[2–4] has driven growing demand for high-performance soft pressure sensors. Capacitive pressure sensors have been widely used due to their advantages, such as high sensitivity, fast signal response, and relatively low power consumption.[5–8] However, these sensors are usually prone to mechanical damage during operation, leading to degraded reliability and reduced lifetime.[9,10] Developing soft capacitive pressure sensors with autonomous self-healing capabilities is imperative to ensuring their reliable performance and long-term durability.

Research on self-healing materials has progressed rapidly, particularly in intrinsic self-healing polymers based on reversible dynamic bond reconstruction,[11,12] including hydrogen bonds,[13–15] $\pi$–$\pi$ stacking,[16,17] ionic interactions,[18,19] metal coordination,[20] and reversible dynamic covalent bonds (such as imine bonds,[21] disulfide bonds[22,23]), etc., which could facilitate reconstruction after physical damage. However, achieving autonomous self-healing under harsh conditions, such as aqueous solution and subzero temperatures, remains challenging because the mobility of polymer chains and the dynamics of reversible bonds are significantly reduced.[22,24,25] In soft pressure sensors, self-healing polymers are often blended with conductive fillers to impart electrical conductivity. Multi-walled CNT has great potential applications in flexible sensors due to its high intrinsic carrier mobility, conductivity and mechanical flexibility.[26–28] However, the incorporation of such fillers can further inhibit self-healing by obstructing dynamic bond reformation and polymer chain realignment.[29] Despite the development of various high-performance self-healing materials, their adoption in soft pressure sensors is usually accompanied by inferior healing efficiency due to the inconsistency of healing rate within the multi-layer architecture. This can cause residual stress or even detachment at interfaces. Therefore, the development of self-healable pressure sensors that can recover both mechanical and electrical properties under diverse environmental conditions remains a significant challenge.

In this work, we designed an all-in-one self-healable soft capacitive pressure sensor based on a chemically modified PDMS. The incorporation of dynamic imine and disulfide bonds enables the elastomer to self-heal not only under ambient conditions, but also in aqueous environments, at subzero temperatures (−15 °C), and in high-concentration saline solution (35 wt% NaCl). An all-in-one soft capacitive pressure sensor with full-module self-healing

J. Guo, L. Zhao, Z. Ouyang, Q. Zuo, Y. Liang
Department of Materials Science and Engineering
Southern University of Science and Technology
No. 1088 Xueyuan Blvd, Shenzhen 518055, China
E-mail: zhaoly@sustech.edu.cn
J. Leng
Center for Composite Materials and Structures
Harbin Institute of Technology
P.O. BOX 3011, No. 2 Yikuang Street, Harbin 150080, China
E-mail: lengjs@hit.edu.cn
The ORCID identification number(s) for the author(s) of this article can be found under https://doi.org/10.1002/adfm.202525419

DOI: 10.1002/adfm.202525419

 

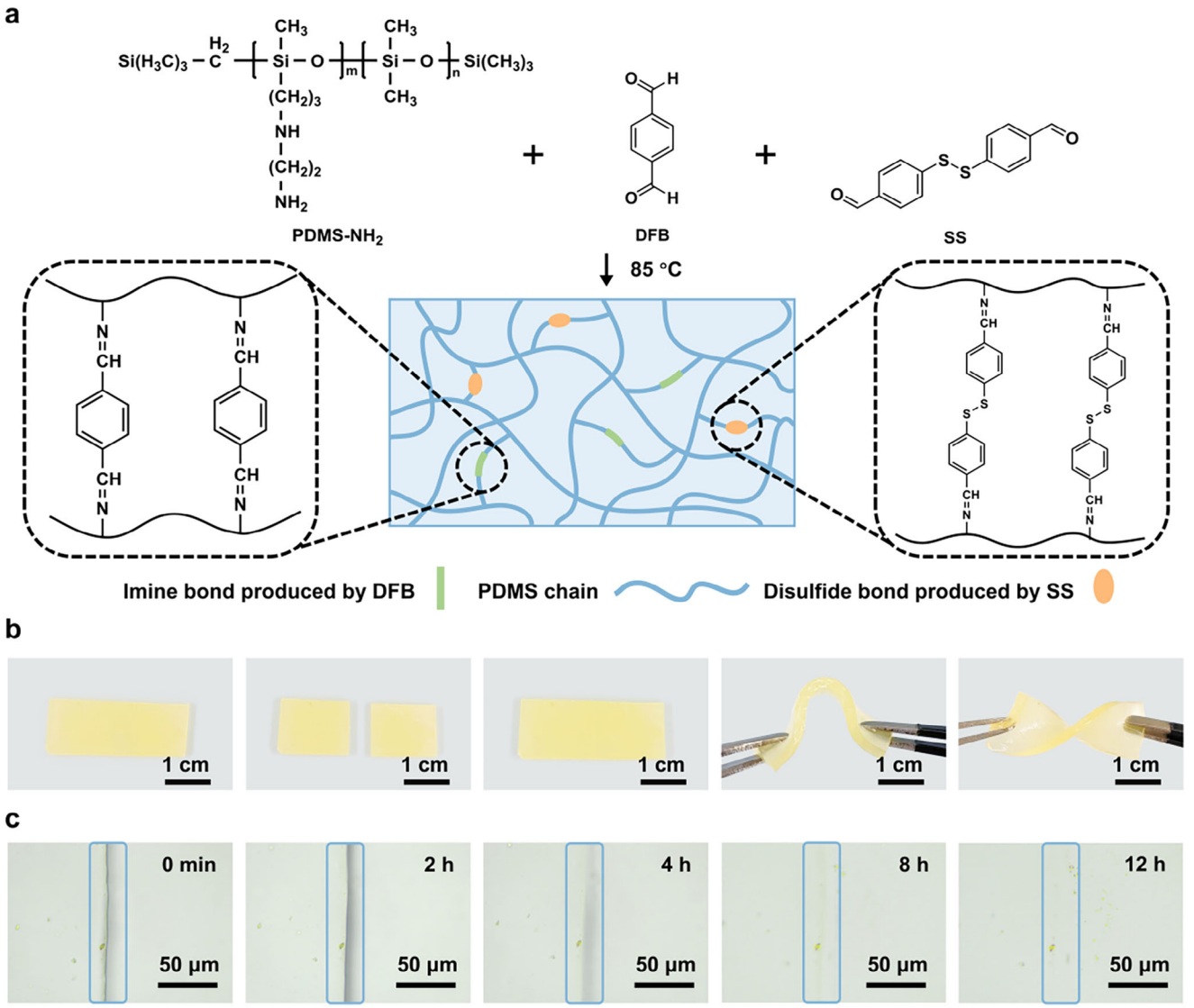


**Figure 1.** Design of the PDMS-$NH_2$/SS-CHO elastomer with autonomous self-healing ability. a) Schematic illustration for the preparation of PDMS-$NH_2$/SS-CHO and the ideal structure of the supramolecular polymer network based on imine and disulfide bonds. b) Photographs showing that the healed polymers can withstand twisting and bending deformations. c) Optical microscope comparison images of the polymer after being cut and the crack self-healing process at room temperature for 0 h, 2 h, 4 h, 8 h, and 12 h.

property and miscible interface between components was assembled. The sensor exhibits not only superior pressure-sensing performance in terms of sensitivity, response time, and cyclic stability but also exceptional performance consistency between pristine and healed devices. The self-healing efficiency of sensor performance is approximately 100% within the range of 0–30 kPa, 93.5% within the range of 30–100 kPa, and 80% within the range of 100–260 kPa at room temperature (RT). Integrating the sensors on soft robotic arms and a submarine model, the sensor consistently recovered stable sensing performance after damage. This all-in-one self-healing sensor shows great promise for applications in extreme environments such as deep-sea and polar regions.

## 2. Results and Discussion

### 2.1. Material Design of Self-Healing Polymer

The schematic of the chemical composition and structure of the as-prepared self-healing polymer is presented in **Figure 1a**. We used amino-terminated polydimethylsiloxane (PDMS-$NH_2$) as the polymer matrix with 1,4-diformylbenzene (DFB) and 1,2-bis[4-(formyl)phenyl]disulfane (SS-CHO) as chain extenders and cross-linkers. The amino groups on PDMS-$NH_2$ side chains undergo Schiff base reactions with aldehyde groups from both DFB and SS-CHO, forming imine bonds[30,31] that establish dynamic cross-linking networks. The intrinsic disulfide bonds[32] in

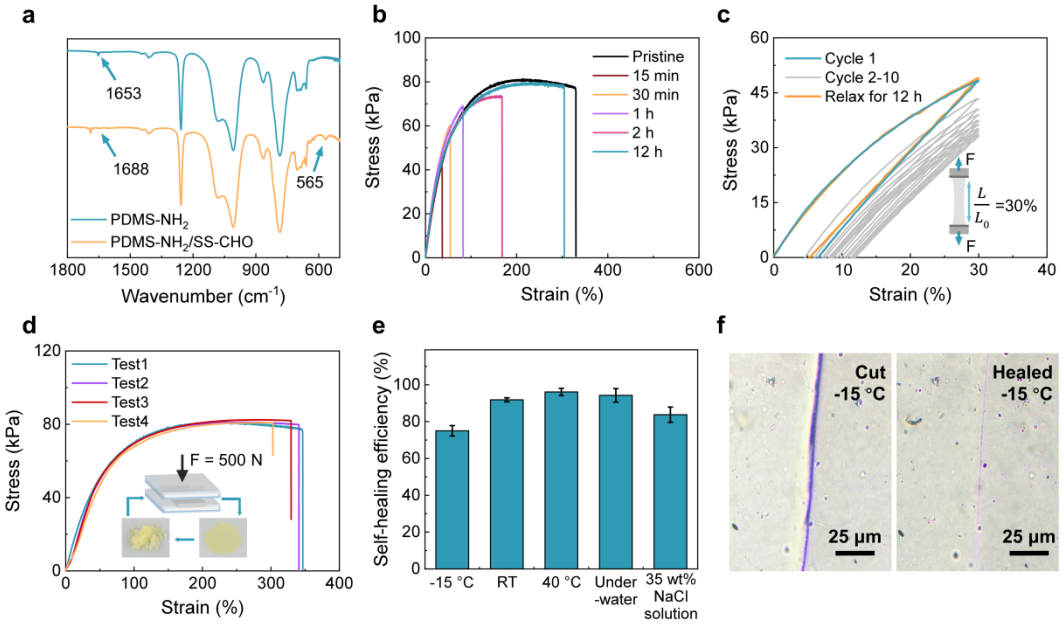


**Figure 2.** The self-healing properties of the polymers. a) FT-IR spectrum of the polymer (with/without SS-CHO groups). b) Stress–strain curves of the specimen healed for different durations at room temperature. Stretching speed is 15 mm min$^{-1}$. c) The stress–strain curve of the pristine polymer in cyclic stress–strain tests (30% strain) during cyclic stretching and releasing. Stretching speed is 10 mm min$^{-1}$. d) The stress–strain curves of the pristine (Test 1) and regenerated PDMS polymer (Test 2–4). Stretching speed is 15 mm min$^{-1}$. e) The self-healing efficiency (%) of specimens healed at −15 °C for 12 h, at room temperature for 12 h, at 40 °C for 12 h, underwater for 12 h, and in 35% NaCl solution at room temperature for 12 h. Stretching speed is 15 mm min$^{-1}$. f) Optical microscope comparison images of the polymer after being cut and the crack self-healing at −15 °C for 24 h.

SS-CHO further contribute to the self-healing capability through dynamic bond exchange. A rectangular polymer specimen was bisected (Figure 1b) and subsequently allowed to heal through interfacial contact autonomously. After 2 h of room-temperature healing, the recombined specimen regained sufficient mechanical integrity to withstand various deformations, including bending and twisting. When the two cut parts contact together, the reversible dynamic bond recombines at the interface, followed by the mutual diffusion and re-entanglement of the polymer chain in the damaged area. Finally, the elastomer completes self-healing and recovers its mechanical properties.[33] According to the optical microscope image observation (Figure 1c), the incision marks on the elastomer were nearly fully eliminated after self-healing for 12 h at room temperature. Through the fluorescence microscopic (Figure S1, Supporting Information) and confocal microscopic images (Figure S2, Supporting Information), the crack has been largely recovered after the healing process. These observations indicate that the synergistic interplay of multiple dynamic bonds (imine and disulfide bonds) enables effective room-temperature self-healing in the as-developed elastomer system.

The successful synthesis of the dual cross-linked polymer was confirmed using Fourier-transform infrared spectroscopy (FT-IR) (**Figure 2a**), and the FT-IR spectrum of the self-healed polymer is shown in Figure S3 (Supporting Information). The characteristic absorption peaks appear at 1650–1670 and 565 cm$^{-1}$, respectively, due to the stretching vibrations of C═N and S—S. Further evidence from 1H NMR spectra is provided in Figure S4 (Supporting Information), the peak observed at $\delta = 8.7$ ppm is associated with the imine bond (—CH═N). These all indicate the successful introduction of imine bonds and disulfide bonds. The self-healing efficiency of the polymer was quantitatively assessed through mechanical characterization, wherein the ratio of self-healing-to-pristine elongation at break served as the primary evaluation metric. In the self-healing test, the pristine polymer specimens were cut into two pieces, and their self-healing properties over different durations were quantitatively evaluated by mechanical tensile tests (Figure 2b). The pristine specimen exhibited a tensile strength of 81.2 kPa and elongation at break of 329.3%, whereas the 12-h healed specimen attained comparable mechanical properties (79.6 kPa tensile strength, 304.4% elongation). The healing efficiency increased progressively from 12.1% (self-healing for 15 min) to 92.4% (self-healing for 12 h), demonstrating autonomous room-temperature self-healing.

The extension and recovery properties are presented in cyclic stretch-release tests (Figure 2c). Progressive reduction in tensile stress accompanied by pronounced hysteresis loops was observed with increasing loading cycles. This mechanical weakening likely originates from partial fracture of reversible dynamic covalent bonds under tensile stress, where continuous cyclic deformation impedes complete bond reformation, causing the tensile stress to decrease as stretching cycles increase. Due to the reversible dynamics of the imine and sulfur bonds in the polymer, the stress-strain curve of the tensile test almost coincides with the first cycle of the cyclic tensile test after the polymer is relaxed at room temperature for 12 h. The inherent reversibility of imine and disulfide bonds facilitated nearly complete reconstruction of fractured covalent networks, thereby restoring the polymer's pristine mechanical properties.[34,35]

The polymer designed in this work exhibits excellent reprocessability at room temperature. The specimen was cut into small pieces and placed between gaskets lined with polytetrafluoroethylene (PTFE) film. After compression molding for 12 h at room temperature under a pressure of 500 N, the reprocessed specimen was obtained. Mechanical tests were performed on the pristine and reprocessed specimens (Figure 2d). The data demonstrate that the mechanical properties of the polymer exhibit minimal changes even after three reprocessing cycles, with the elongation at break retaining 87.4% of its initial value. We also implemented repeated "cutting-healing" processes on the same region of the specimens (Figure S5, Supporting Information). After 10 cycles, the elastomer still retained a self-healing efficiency of 80%, demonstrating good self-healing repeatability. These results validate that strong bonding could be formed uniformly and isotropically at the contact interface between the as-prepared modified PDMS patches and provide an effective bottom-up approach for additive manufacturing.

Furthermore, we evaluated the self-healing capabilities of the polymer in various conditions, including freezing (−15 °C), heating (40 °C), underwater, and in a saline solution (35 wt% NaCl solution at RT) (Figure 2e). At 40 °C, the self-healing efficiency reached 96.12% ± 1.97%. At sub-zero temperature (−15 °C), the efficiency attained 75.01% ± 2.83%. The material exhibits notable self-healing capabilities in low-temperature environments, driven by synergistic interactions of multiple reversible dynamic covalent bonds within the polymer network. Following damage, polymer chain reorganization facilitates interfacial reconfiguration at fracture surfaces. Notably, disulfide bonds exhibit enhanced reconnection efficacy at reduced temperatures, attributed to their low bond dissociation energy (60 kcal $mol^{-1}$),[19] facilitating interfacial bond reformation at low temperature,[36,37] which further ensures the easy reconnection at freezing conditions. Subsequent submersion in aqueous environments (room temperature, 12 h) yielded 94.29 ± 3.67% healing efficiency, while immersion in 35 wt% NaCl solution achieved an efficiency of 83.76 ± 4.16%. Polymers still have a high self-healing efficiency underwater. This might be because the polymer backbone (PDMS) gives rise to water-insensitive self-healing.[38] The hydrophobic property induces the orderly arrangement of surrounding water molecules, thereby reducing entropy. To a certain extent, it avoids interfering with the reversible dynamic bond reconstruction in the elastomer.[22,39,40] Among the self-healing environmental conditions mentioned above, cracks can be well recovered in both underwater conditions (Figure S6, Supporting Information) and 35 wt% NaCl solution (Figure S7, Supporting Information), while the self-healing efficiency is the lowest at −15 °C. After storing the specimen at −15 °C for 2 h, we cut it and place it back in −15 °C for self-healing. After self-healing for 24 h, the incision marks on the polymer almost disappeared (Figure 2f). The self-healing polymer designed in this work still has a good self-healing result even under the low-temperature conditions, with the lowest self-healing efficiency. Such robust healing performance in complex environments holds critical implications for marine and polar applications.

### 2.2. Preparation of Self-Healing Conductive Composites

The synthesis pathway and raw material composition of the conductive polymer are detailed in Figure S8 (Supporting Information). PDMS-$NH_2$ was blended with SS-CHO in toluene solvent under reflux at 85 °C for 3 h. Multi-walled CNT, PEDOT:PSS and Triton X-100 (the introduction of Triton X-100 can relieve the interfacial tension between the two phases, making PDMS and PEDOT:PSS blend easier[41]) were dispersed via ultrasonic treatment for 2 h by using an ultrasonic cell crusher. Subsequent addition of DFB to the homogenized mixture yielded conductive gel precursors. Solvent evaporation was completed in a vacuum oven, followed by room-temperature compression molding to obtain the final polymer products.

The introduction of conductive fillers affects the self-healing efficiency and mechanical properties of the self-healing polymer. As mere CNT incorporation was observed to diminish self-healing efficiency (Figure S9, Supporting Information), we used the PEDOT:PSS as a co-blender to change it. Upon introducing PEDOT:PSS, hydrogen bonding formed between PEDOT:PSS chains and the polymer matrix (**Figure 3a**; Figure S10, Supporting Information). These hydrogen interactions, recognized as predominant reversible bonds in self-healing systems, synergize with two other dynamic bonds to enable effective healing.[40,42] PEDOT:PSS loading induced mechanical property alterations of CNT-doped samples (Figure S11, Supporting Information), increasing elongation at break while reducing ultimate tensile strength with the rise of dosage. Excessive PEDOT:PSS (>25 wt%) caused component migration at fracture interfaces,[43] degrading healing efficiency (Figure S12, Supporting Information). Thus, 25 wt% PEDOT:PSS was established as the optimal concentration. After adding 25 wt% PEDOT:PSS, the mechanical properties of conductive polymers doped with different CNT contents are shown in Figure S13 (Supporting Information). When the conductive elastomer was divided in half, bisected specimens demonstrated autonomous interfacial reconstruction under ambient conditions (self-healing for 12 h), achieving mechanical integrity sufficient for bending/twisting deformations (Figure 3b). The conductive elastomer obtained in this way can also achieve self-healing at subzero temperatures (−15 °C) and aqueous environment. As shown in Figures S14 and S15 (Supporting Information), the elastomers were cut off, and the broken surface was reattached at −15 °C and underwater. After self-healing under the corresponding environmental conditions for 12 h, the conductive elastomers were able to reconnect.

Based on the above-mentioned self-healing polymer and its nanocomposites, as well as the relatively uniform dispersion of CNT in the composites (Figure S16, Supporting Information), we developed a capacitive soft pressure sensor utilizing the polymer for both electrode and dielectric layers. The electrode and dielectric layer fabrication was achieved through different CNT loading within the self-healing matrix (with 25 wt% PEDOT:PSS in all conductive elastomers). The 3 wt% CNT/25 wt% PEDOT:PSS/PDMS composite's relative permittivity (16.7) is significantly higher than that of pure PDMS (2.8). Thereby, the capacitance change under pressure could be amplified, thus the sensitivity of the capacitive pressure sensor is improved. With the

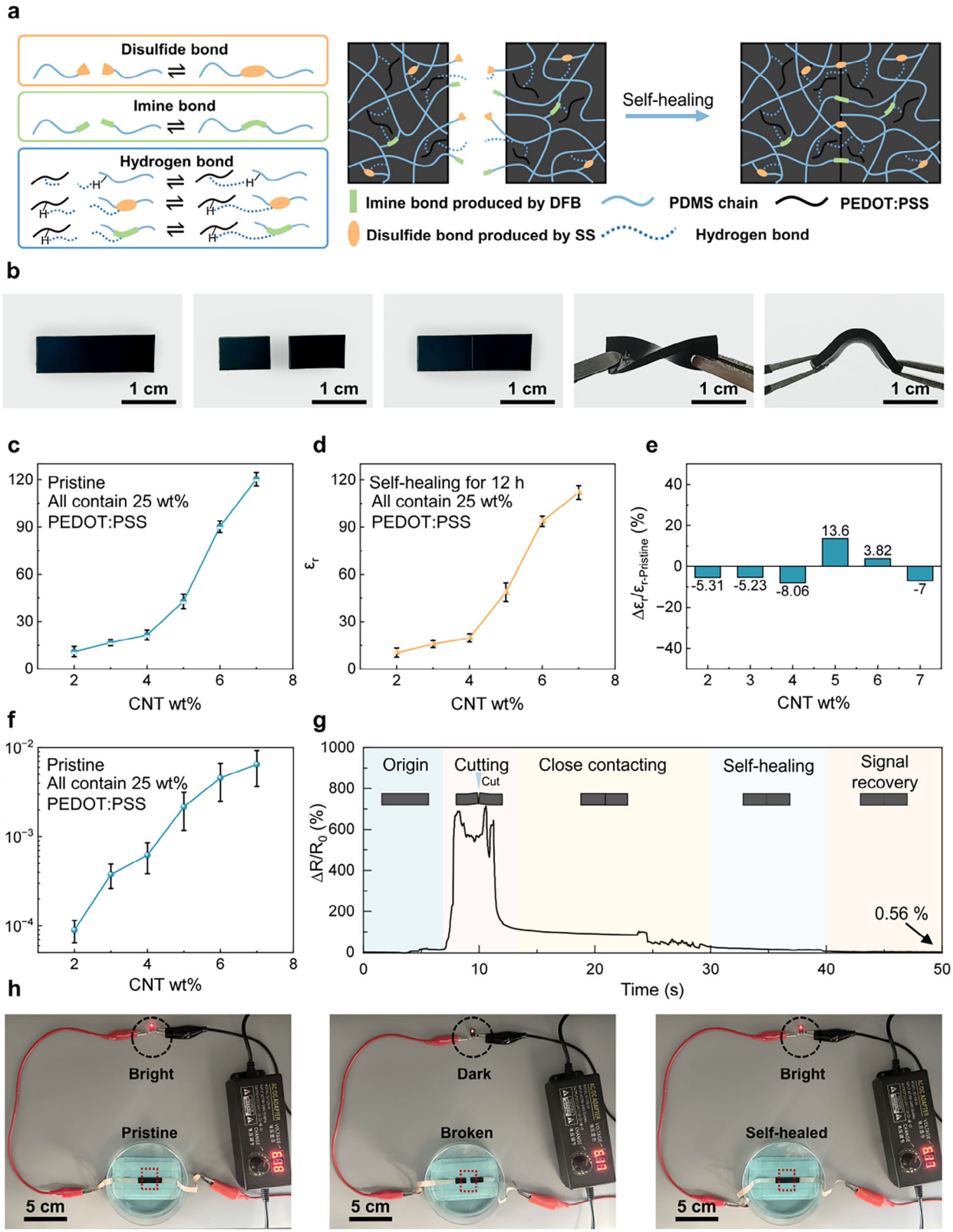

increase of CNT concentration, the permittivity of the nanocomposite shows a dramatic rise (Figure 3c). And this trend remains after a cutting and self-healing process for 12 h (Figure 3d). The rate of change in dielectric constant (Figure 3e) of pristine and self-healing conductive elastomers is relatively low. Among them, the rate of change in dielectric constant of 3 wt% CNT conductive elastomer is only −5.23%. Also, increasing CNT content enhanced conductive film conductivity (Figure 3f) while compromising healing efficiency. We tested the resistance curve of conductive elastomer films containing 6 and 7 wt% CNT during cutting and self-healing (Figure 3g; Figure S17, Supporting Information). Following complete blade severing and interfacial contact restoration, the 6 wt% CNT film basically restored baseline electrical signals within 40 s with a resistance change rate of only 0.56%. For the nanocomposite film with 7 wt% CNT, after restoring interface contact and self-healing for 12 h, the resistance change of this film still remained at 7.1%. The self-healing effect of the electrical signal of the 6 wt% CNT film was significantly better than that of the 7 wt% CNT film. This phenomenon is attributed to CNT-induced restriction of polymer segment mobility, impeding molecular chain realignment.[29] Healing performance is governed by polymer network diffusion dynamics and reversible bond reformation.[44] Elevated CNT concentrations promote nanoparticle aggregation during synthesis,[45] hindering polymer chain re-entanglement and dynamic bond reconnection at damaged interfaces. The 6 and 7 wt% CNT composites exhibited conductivities of 0.0046 and 0.0065 S $m^{-1}$, respectively. Considering electrical self-healing efficiency, the 6 wt% CNT formulation was selected for electrode fabrication. Consequently, the finalized self-healing capacitive sensor employs PDMS-$NH_2$ doped with 6 wt% CNT as electrodes and 3 wt% CNT as dielectric layers.

To further demonstrate the self-healing performance of the conductive material in electrical signals, we connected a power source, a light-emitting diode (LED), and a self-healing conductive elastomer in air and underwater to form a simple circuit. As shown in Figure S18 (Supporting Information), the LED emitted a bright light at a voltage of 6.17 V. After cutting the conductive elastomer in half, the circuit was disconnected, and the LED turned off. After recontacting the cut surface of the conductive elastomer in air, it performed a rapid self-healing, and the LED was bright again. We also placed the self-healing conductive elastomer underwater and demonstrated a similar self-healing of electrical signals. As shown in Figure 3h, the LED emitted light at around 6.17 V. After cutting the elastomer underwater, the LED quickly dimmed. After recontacting the cut surface of the conductive polymer underwater and self-healing for 12 h, the circuit was restored to a conductive state, and the LED was bright again. The ability to self-heal electrical signals underwater expands the application range of self-healing materials in the field of flexible sensors.

### 2.3. Sensing Properties of Multilayered Self-Healing Homogeneous Soft Capacitive Pressure Sensor

In this work, to increase the deformation of the dielectric layer and the effective contact area, we chose the micro-dome structure as the microstructure in the sensor. With the decrease of microdome size, a higher sensitivity of the device could be achieved (Figure S19, Supporting Information). We used a high-precision 3d printer to create the microstructure template of the dielectric layer, and fabricated the microstructured dielectric layer of the device by the embossed method (Figure S20, Supporting Information). The introduction of microstructure enables the sensor to have higher sensitivity and a wider response range (Figure S21, Supporting Information).[46] Given the compromised stability of single-layer dielectric configurations (Figures S22 and S23, Supporting Information), the electrode and dielectric layers were assembled following the architecture in **Figure 4a** through systematic evaluation. Scanning electron microscopy (SEM) imaging confirmed the dielectric microstructure and the device's cross-sectional morphology (Figure 4b). Since all modules of the capacitive soft pressure sensor, including the substrate, electrode, and dielectric layer, are based on the self-healable polymer, an all-in-one self-healable device was achieved. Bisected sensor segments underwent healing through interfacial contact. After self-healing for 24 h, the self-healed device could be elongated without breaking (Figure 4c).

This homogeneous soft capacitive pressure sensor with full-module self-healing function showed reliable and consistent performance before and after repair. The self-healable sensor has an operational range of 0–260 kPa (Figure 4d). Notably, in a low-pressure range of 0–30 kPa, the sensor shows good sensitivity, reaching 0.130 $kPa^{-1}$. Using the ratio of sensitivity between the self-healing and pristine sensor as the primary evaluation metric for the self-healing efficiency, the performance within the range of 0–30 kPa is ≈100%, 93.5% for the range of 30–100 kPa, and 80% for the range of 100–260 kPa. With the increase of pressure, there's a slight decrease in sensitivity for the healed sensor compared with the pristine sensor, which could be attributed to the incomplete recovery of stretchability after healing. But in general, the pressure sensing performance has been well restored after healing, which meets the application's demand for signal consistency. Under 5 kPa loading (Figure 4e), pristine sensors exhibited a response time of 114 ms and a recovery time of 93 ms, while the healed sensor displayed similar response (112 ms) and recovery (95 ms) times. These response/recovery kinetics remained

**Figure 3.** The properties of the conductive nanocomposite based on the self-healing polymer. a) Schematic illustration of the self-healing mechanism of the conductive elastomers. b) Photographs showing the healed conductive elastomer (contains 3 wt% CNT and 25 wt% PEDOT:PSS) withstanding twisting and bending deformations. c) Dielectric constant diagram of conductive elastomers with a doping ratio of 2 to 7 wt% CNT (all elastomers contain 25 wt% PEDOT:PSS). d) Dielectric constant diagram of conductive elastomers with a doping ratio of 2 to 7 wt% CNT after cutting and self-healing for 12 h (all elastomers contain 25 wt% PEDOT:PSS). e) Diagram showing the change in the dielectric constant of conductive elastomers with a doping ratio of 2 to 7 wt% CNT after cutting and self-healing for 12 h (all elastomers contain 25 wt% PEDOT:PSS). f) Conductivity diagram of conductive elastomers with a doping ratio of 2 to 7 wt% CNT (all elastomers contain 25 wt% PEDOT:PSS). g) Change in the resistance of conductive elastomer during self-healing after cutting. h) The self-healable conductive elastomer placed underwater when connected with an LED in series, demonstrating luminescence recovery of the LED after self-healing for 12 h.

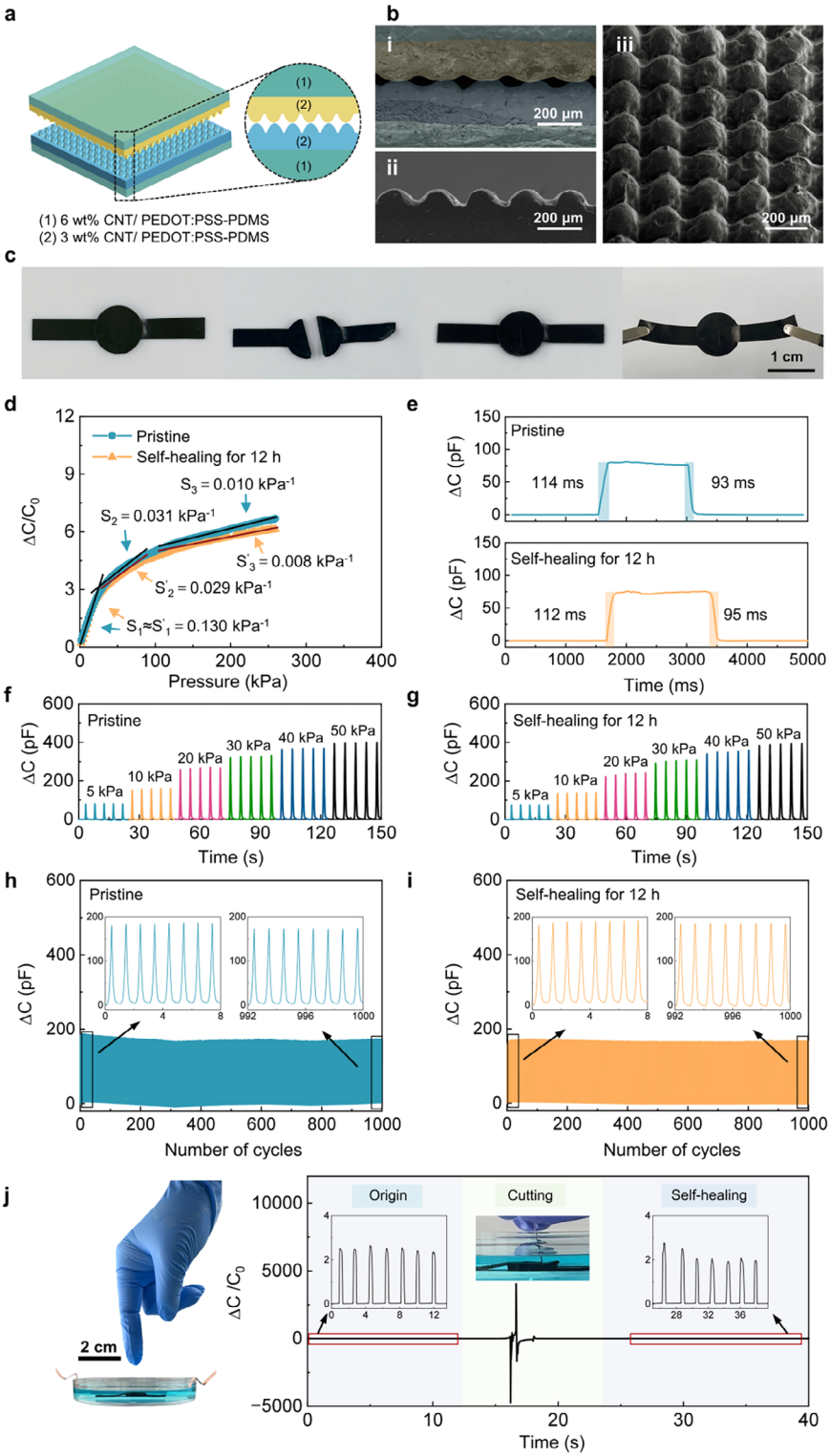


**Figure 4.** Properties of self-healable capacitive soft pressure sensors at room temperature and underwater. a) Structural illustration of a self-healing capacitive soft pressure sensor. b) SEM image of the layered structure of a capacitive soft pressure sensor. (i) Sectional view of the sensor. (ii) Sectional view of the dielectric layer with microstructure. (iii) Top view of the dielectric layer with microstructure. c) Photographs of the healed sensor withstanding stretching. d) Relative capacitance change along with the pressure range for both pristine and healed states of the sensor. e) The response and recovery time of the sensor before and after self-healing. f,g) Step response (f) and stability analysis (g) for sensors subjected to pressures of 5, 10, 15, and 20 kPa. h,i) The durability of the sensor at a pressure level of ≈10 kPa in the pristine (h) and healed (i) conditions over 1000 cycles. j) Capacitance change of the pristine and healed sensor placed underwater.

consistent pre-/post-healing, and all surpassed human tactile perception latency (139 ms).[47,48] Pressure discrimination capability was evaluated through stepwise loading-unloading cycles across 0–50 kPa ranges. The change in capacitance (ΔC) of the sensor remains stable with varying forces (Figure 4f), and this property is maintained after the healing process (Figure 4g). A constant pressure of ≈10 kPa was applied to the pristine and self-healing sensors for 1000 loading-unloading cycles (Figure 4h,i), and the signals of both sensors showed superior consistency and stability, meeting the application requirements of the self-healing sensors. To evaluate the sensor's repeatability in healing, we implemented multiple cutting-healing processes on the sensor and compared the pressure sensing performance between the pristine state and after certain cutting-healing cycles. As shown in Figure S24 (Supporting Information), the sensor's response towards a 5 kPa pressure resembles that in the pristine state when no >10 healing cycles are implemented. After 15 times healing, there's a slight baseline shift as well as variation in responsivity. Therefore, we suppose the maximum number of self-healing for the recovery of the sensor's functionality is 10.

To verify whether the sensor can restore the sensing signal underwater, we immersed the sensor in water. As shown in Figure 4j, by applying pressure to the underwater sensor, the sensor responded with a spike. After damaging the sensor for a short time, the sensing signal basically recovered. The ability to restore the signal underwater lies the foundation for the application of sensors with self-healing functions in extreme environments such as the ocean. Compared with the state-of-the-art reported self-healable capacitive pressure sensors (Table S1, Supporting Information),[10,49–55] our sensor has a competitive performance in terms of response range, sensitivity and self-healing efficiency. Besides, the versatile conditions for the healing process, including underwater, ultralow temperature, and high-concentration saline solutions, enable our sensor to have great potential in practical operation scenarios.

### 2.4. Sensor Application Scenario Demonstration

We demonstrated the application potential of the sensor by attaching the sensor to a soft robotic gripper as a force gauge (**Figure 5a**) to record signals when grasping different objects in a variety of working scenarios. We used soft robotic grippers containing sensors to respectively grab a soft doll (Figure 5b), a cuboid-shaped box (Figure S25, Supporting Information), and a cactus (Figure 5c). For the spherical doll, since its surface is smooth, the sensor's signal is relatively stable. For a cactus, with its surface covered in many sharp spines, the sensor first contacts them during grasping before lifting the cactus, causing a small peak in the sensing signal at the initial stage. The differences in the signal patterns when grasping different objects effectively reflect the actual behavior of the gripper, indicating the sensor's capability in materials recognition.

Since the soft robotic gripper undergoes severe shear force in operation, the attached sensor is susceptible to mechanical damage. To this end, the self-healing property of the sensor was essential for durable use in such a scenario, which was investigated thoroughly. The sensor was attached to one end of the soft robotic gripper, and a needle was attached to the other end of the gripper. When the two gripper ends approach, the tip of the needle touches the sensor and then detaches (Figure 5d). When a large force is applied, the needle tip penetrates the sensor, causing signal disturbance. After 24 h of self-healing at room temperature, the signal response almost recovered to that before self-healing. The results show that the sensor has a good advantage in the working environment where sharp objects are grasped or touched. To simulate the possible damage in the actual application process, the mechanical gripper attached to the sensor keeps grabbing the glass fragments in the pile of broken glass (Figure 5e). Due to the different shapes of the captured fragments, the signal is slightly different for various grasping processes. When the sharp, broken glass damages the sensor, the sensing signal is disturbed. However, after 24 h of self-healing, the glass fragments are picked up again, and the signal is basically restored. This further confirms the application prospect of a homogenous capacitive soft pressure sensor, which can realize self-healing in the field of remote intelligent robots and human-computer interaction.

To demonstrate the practical application potential of the sensor as a force gauge for the underwater robot, we attached the sensor to the tip of a submarine model to investigate its underwater sensing performance. As shown in Figure 5f, when the submarine model tip made a weak or strong impact on the wall of the container, different sensing signals can be obtained, respectively (Figure 5g). After using a knife to scratch the sensor and complete the self-healing, the sensor still exhibits excellent sensing signal response to the same impact from the submarine model tip Figure 5h). This not only confirms that the sensor has underwater sensing performance but also verifies that the sensor has the self-healing capability of underwater sensing signals, demonstrating its application potential in the deep-sea scenario.

## 3. Conclusion

In summary, we developed a novel self-healing material by incorporating two types of reversible dynamic bonds—imine and disulfide bonds—into a cross-linked polymer network, enabling efficient structural reassembly after damage. This material system exhibits excellent self-healing performance under various environments, including not only ambient conditions, but also harsh aqueous conditions at subzero temperatures (−15 °C), and in high-concentration saline solution (35 wt% NaCl). Based on this material, a homogeneous soft capacitive pressure sensor with full-module self-healing capability was fabricated. Both the original and healed sensors exhibit outstanding sensing performance, including a fast response time of ≈113 ms, a sensitivity of 0.130 $kPa^{-1}$ in the 0–40 kPa range, and a broad detection range extending to 260 kPa. The effective cross-link density of PDMS-$NH_2$/SS-CHO elastomer is about 23 $mol/m^3$. The self-healing efficiency reaches ≈100% in the 0–30 kPa range, 93.5% in 30–100 kPa, and 80% in 100–260 kPa, indicating nearly complete functional recovery and meeting practical requirements for signal consistency before and after healing. Furthermore, the sensor was integrated into soft robotic grippers and a submarine model, where it consistently restored stable sensing performance after damage. The combination of wide-range high-resolution sensing and efficient autonomous self-healing underscores its strong

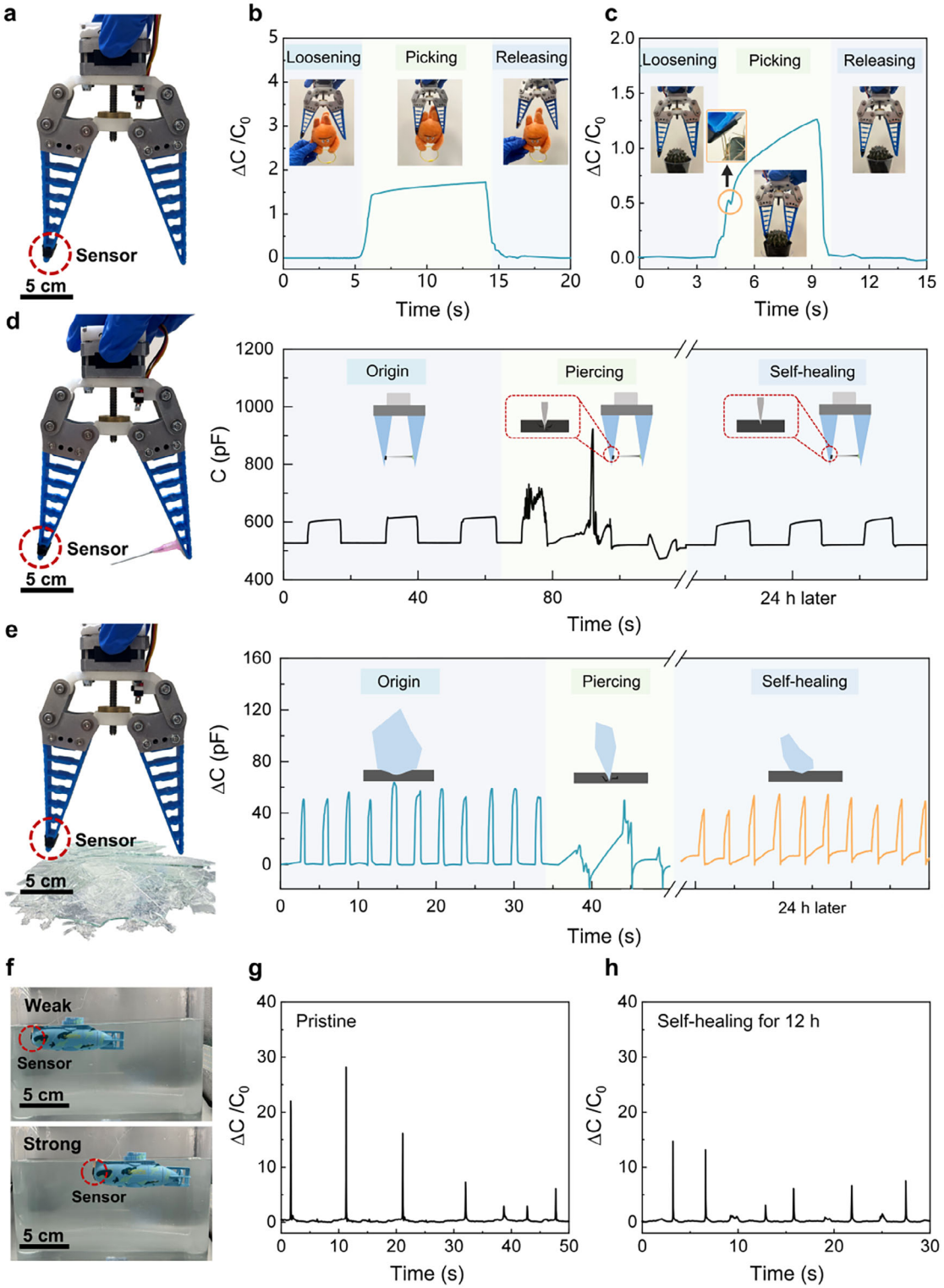


**Figure 5.** Demonstration of the self-healable sensor functioning as a force gauge of load-bearing devices. a) Photograph of the sensor attached to the soft robotic gripper. b) The sensor's signal in the process of grasping the doll. c) The sensor's response in the process of grasping the cactus. d) The sensor's response before and after the sensor is damaged and self-healing at room temperature for 24 h when the needle punctures the sensor due to different forces in the grasping process. e) The signal of the sensor after being punctured by sharp glass and self-healing at room temperature for 24 h in the process of grasping glass. f) Photographs of a submarine model tip experiencing strong and weak impacts with an underwater object (wall of the container). g) The responses of the pristine sensor upon impact with an underwater object (wall of the container). h) The responses of a healed sensor upon impact with an underwater object (wall of the container).

potential for practical stress-monitoring applications in extreme environments, such as deep-sea and polar regions.

## 4. Experimental Section

*Materials*: All reagents were commercially available and used as supplied without further purification. Amino-modified PDMS (OFX-8040A, 800–5000 cPs) was purchased from XIAMETER. 4,4′-Disulfanediyldibenzaldehyde ($C_{14}H_{10}O_2S_2$, 95%) was purchased from BIDE. 1,4-diformylbenzene ($C_8H_6O_2$, 99%) and Sodium chloride (NaCl) were purchased from Macklin. Toluene ($C_7H_8$, 99.5%) was purchased from Yonghua Chemical Co., Ltd (China). Multi-walled carbon nanotubes (CNT, length 10–20 µm, 95%) were purchased from XFNAN. Triton X-100 was purchased from Sigma-Aldrich. PEDOT:PSS was purchased from Heraeus.

*Synthesis of Self-Healing PDMS Elastomer*: There were PDMS-$NH_2$ (5 g) and toluene (15 ml) stirred at room temperature for 20 min, 4,4′-disulfanediyldibenzaldehyde (20 mg) was added to it, followed by ultrasonic dispersion for 5 min. The above dispersion was stirred continuously at 85 °C for 3 h. DFB (250 mg) was added to toluene (25 mL) and stirred at room temperature for 20 min. This solution (3 mL) was added to the above PDMS dispersion and stirred continuously until the organogel was obtained. The organogel was placed in a vacuum and dried at 60 °C for 24 h to remove residual solvent. Finally, the material was placed between gaskets with PTFE films, and a hot press machine was used to press at 500 N pressure at room temperature for 12 h to obtain the self-healing PDMS elastomer. The effective cross-link density of PDMS-$NH_2$/SS-CHO elastomer is about 23 mol $m^{-3}$.

*Synthesis of Self-Healing PDMS/CNT/PEDOT:PSS Composites*: There were PDMS-$NH_2$ (5 g) and toluene (15 ml) stirred at room temperature for 20 min, 4,4′-disulfanediyldibenzaldehyde (20 mg) was added to it, followed by ultrasonic dispersion for 5 min. The above dispersion was stirred continuously at 85 °C for 3 h. Different mass fractions of CNT relative to PDMS-$NH_2$, 25 wt% PEDOT:PSS relative to PDMS-$NH_2$, Triton X-100 (0.4 g), and toluene (20 mL) were added to the above PDMS dispersion, followed by ultrasonic dispersion for 2 h in an ice-water bath. Then, DFB (250 mg) was added to toluene (25 mL) and stirred at room temperature for 20 min. This solution (3 mL) was added to the above PDMS/CNT/PEDOT:PSS dispersion and stirred continuously until the conductive organogel was obtained. The conductive organogel was placed in a vacuum and dried at 60 °C for 24 h to remove residual solvent. Finally, the material was placed between gaskets with PTFE films, and a hot press machine was used to press at 500 N pressure at room temperature for 12 h to obtain self-healing PDMS/CNT/PEDOT:PSS composites.

*Characterization*: The self-healing condition at the damaged sites of the materials was determined using an optical microscope (Leica DM750 M, Leica Microsystems, Germany) equipped with a digital camera (Flexacam C3). The chemical structures of the synthesized self-healing polymers were characterized by Fourier transform infrared spectroscopy (FTIR, Frontier, PerkinElmer Inc., USA). Ultrasonic dispersion was performed using an ultrasonic cell disruptor (SCIENTZ-950E, Ningbo Scientz Biotechnology Co., Ltd., China) operated at 120 W output power in pulsed mode (4 s on, 4 s off). The materials were pressed using a hot press (VHP-5T-4, Hefei Kejing Material Technology Co., Ltd., China). The mechanical properties and self-healing efficiency of the samples were measured with a universal testing machine (LE3153, Shanghai Lishi Instruments Co., Ltd., China). The dielectric constants of elastomers doped with different mass fractions of CNTs were determined using an impedance analyzer (4294A, Agilent Technologies, USA). The electrical conductivity of elastomers doped with different mass fractions of CNTs was measured with a four-probe tester (GSZ-RTS-9, Beijing Heng Odd Instrument Co., Ltd., China). Capacitance and resistance values were tested using an LCR meter (E4980AL, Keysight Technologies, USA). A microstructural template for the dielectric layer was fabricated using a 3D printer (MAX X27, Asiga Pty Ltd., Australia). The sectional view of the sensor and the sectional/top views of the dielectric layer microstructures were characterized by field emission scanning electron microscopy (FESEM, MIRA3, TESCAN Brno s.r.o., Czech Republic).

## Supporting Information

Supporting Information is available from the Wiley Online Library or from the author.

## Acknowledgements

Jiaxin Guo and Lingyu Zhao contributed equally to this work. The work was funded by the Natural Science Foundation of Guangdong Province (2023A1515012835), Basic Research Program of Shenzhen (JCYJ20230807093559046), and National Natural Science Foundation of China (92471203, 52103301).

## Conflict of Interest

The authors declare no conflict of interest.

## Data Availability Statement

The data that support the findings of this study are available from the corresponding author upon reasonable request.

## Keywords

all-in-one structure, harsh environments, self-healing property, soft pressure sensor, underwater robotics

Received: September 23, 2025
Revised: November 17, 2025
Published online: December 5, 2025

[1] Y. Luo, M. R. Abidian, J.-H. Ahn, D. Akinwande, A. M. Andrews, M. Antonietti, Z. Bao, M. Berggren, C. A. Berkey, C. J. Bettinger, J. Chen, P. Chen, W. Cheng, X. Cheng, S.-J. Choi, A. Chortos, C. Dagdeviren, R. H. Dauskardt, C.-A. Di, M. D. Dickey, X. Duan, A. Facchetti, Z. Fan, Y. Fang, J. Feng, X. Feng, H. Gao, W. Gao, X. Gong, C. F. Guo, et al., *ACS Nano* **2023**, *17*, 5211.
[2] N. Dai, I. M. Lei, Z. Y. Li, Y. Li, P. Fang, J. W. Zhong, *Nano Energy* **2023**, *105*, 108041.
[3] L. X. Ye, F. Wu, R. X. Xu, D. Zhang, J. J. Lu, C. L. Wang, A. J. Dong, S. C. Xu, L. J. Xue, Z. X. Fan, L. J. Xu, K. F. Li, D. Li, A. Kursumovicg, R. Zhao, R. J. Tang, Q. Lei, H. Y. Wang, J. L. MacManus-Driscoll, Q. S. Jing, *Nano Energy.* **2023**, *112*, 108460.
[4] D. V. Nguyen, P. A. Song, F. Manshaii, J. Bell, J. Chen, T. Dinh, *ACS Nano* **2025**, *19*, 6663.
[5] Y. C. Huang, Y. Liu, C. Ma, H. C. Cheng, Q. Y. He, H. Wu, C. Wang, C. Y. Lin, Y. Huang, X. F. Duan, *Nat. Electron.* **2020**, *3*, 59.
[6] D. Yang, R. L. Yang, F. Y. Liu, J. H. Zhao, D. H. Qu, M., Chen, *Chem.-Eur. J.* **2025**, *31*, 202500407.
[7] H. Z. Wang, Z. Li, Z. Y. Liu, J. K. Fu, T. Y. Shan, X. Y. Yang, Q. Y. Lei, Y. J. Yang, D. H. Li, *J. Mater. Chem. C* **2022**, *10*, 1594.
[8] S. B. Kang, J. Lee, S. Lee, S. Kim, J. K. Kim, H. Algadi, S. Al-Sayari, D. E. Kim, D. Kim, T. Lee, *Adv. Electron. Mater.* **2016**, *2*, 1600356.
[9] M. Kaltenbrunner, T. Sekitani, J. Reeder, T. Yokota, K. Kuribara, T. Tokuhara, M. Drack, R. Schwödiauer, I. Graz, S. Bauer-Gogonea, S. Bauer, T. Someya, *Nature* **2013**, *499*, 458.
[10] C. B. Cooper, S. E. Root, L. Michalek, S. Wu, J.-C. Lai, M. Khatib, S. T. Oyakhire, R. Zhao, J. Qin, Z. N. Bao, *Science* **2023**, *380*, 935.
[11] B. R. Li, P. F. Cao, T. Saito, A. P. Sokolov, *Chem. Rev.* **2023**, *123*, 701.

[12] D. Yang, J. H. Zhao, F. Y. Liu, M. Chen, D. H. Qu, *Chem. Sci.* **2025**, *16*, 9143.
[13] X. Y. Dai, Y. H. Wu, Q. H. Liang, J. K. Yang, L.-B. Huang, J. Kong, J. H. Hao, *Adv. Funct. Mater.* **2023**, *33*, 2304415.
[14] F. Y. Sun, L. F. Liu, T. Liu, X. B. Wang, Q. Qi, Z. S. Hang, K. Chen, J. H. Xu, J. J. Fu, *Nat. Commun.* **2023**, *14*, 130.
[15] F. Yuan, D. H. Li, H. Y. Li, B. Yu, Y. Wei, X. L. Deng, Y. Y. Zhang, W. X. Multi-Compatible, *Adv. Mater.* **2025**, *37*, 2500272.
[16] S. Burattini, B. W. Greenland, D. H. Merino, W. G. Weng, J. Seppala, H. M. Colquhoun, W. Hayes, M. E. Mackay, I. W. Hamley, S. J. Rowan, *J. Am. Chem. Soc.* **2010**, *132*, 12051.
[17] C. Tian, J. Y. Ning, Y. Y. Yang, F. H. Zeng, L. Huang, Q. Liu, J. H. Lv, F. Q. Zhao, Q. B. Kong, X. F. Cai, *Chem. Eng. J.* **2022**, *429*, 132447.
[18] Z. Liu, P. Hong, Z. Y. Huang, T. Zhang, R. J. Xua, L. J. Chen, H. P. Xiang, X. X. Liu, *Chem. Eng. J.* **2020**, *387*, 124142.
[19] J. F. Shi, N. Zhao, D. Y. Yan, J. H. Song, W. X. Fu, Z. B. Li, *J. Mater. Chem. A* **2020**, *8*, 5943.
[20] C.-H. Li, J.-L. Zuo, *Adv. Mater.* **2020**, *32*, 1903762.
[21] P. Wang, Z. C. Wang, L. Liu, G. B. Ying, W. X. Cao, J. Q. Zhu, *Molecules* **2023**, *28*, 6049.
[22] H. S. Guo, Y. Han, W. Q. Zhao, J. Yang, L. Zhang, *Nat. Commun.* **2020**, *11*, 2037.
[23] W. J. Yang, Y. L. Zhu, T. X. Liu, D. Puglia, J. M. Kenny, P. W. Xu, R. Zhang, P. M. Ma, *Adv. Funct. Mater.* **2023**, *33*, 2213294.
[24] T.-P. Huynh, M. Khatib, H. Haick, *Adv. Mater. Technol.* **2019**, *4*, 1900081.
[25] Z. Y. Kong, E. K. Boahen, D. J. Kim, F. L. Li, J. S. Kim, H. Kweon, S. Y. Kim, H. Choi, J. Zhu, W. B. Ying, D. H. Kim, *Nat. Commun.* **2024**, *8*, 2129.
[26] Y. Zhang, X. Zhou, N. Zhang, J. Zhu, N. Bai, X. Hou, T. Sun, G. Li, L. Zhao, Y. Chen, L. Wang, F. Guo, *Nat. Commun.* **2024**, *15*, 3048.
[27] L. B. Hu, D. S. Hecht, G. Grüner, *Chem. Rev.* **2010**, *110*, 5790.
[28] X. R. Yan, J. W. Gu, G. Zheng, J. Guo, A. M. Galaska, J. F. Yu, M. A. Khan, L. Y. Sun, D. P. Yong, Q. Y. Zhang, S. Y. Wei, Z. H. Guo, *Polymer* **2016**, *103*, 315.
[29] Y. H. Zhou, L. Lei, B. Yang, J. B. Li, J. Ren, *Polym. Test.* **2018**, *68*, 34.
[30] J. Zhang, M. K. Xu, N. Zhang, L. M. Tao, M. C. Shao, T. M. Wang, Z. H. Yang, Q. H. Wang, Y. M. Zhang, *Small* **2024**, *20*, 2406358.
[31] G. P. Carden, M. L. Martins, G. Toleutay, S. R. Ge, B. R. Li, S. Zhao, A. P. Sokolov, *Macromol* **2024**, *57*, 8621.
[32] G. Y. Li, S. H. Li, J. Ahmed, W. Tian, L. Li, *InfoMat* **2024**, *6*, 12594.
[33] S. Wang, M. W. Urban, *Nat. Rev. Mater.* **2020**, *5*, 562.
[34] C. Lv, J. K. Wang, Z. X. Li, K. F. Zhao, J. P. Zheng, R. Degradable, *Composites, Part B* **2019**, *177*, 107270.
[35] S. Wang, S. Q. Ma, Q. Li, W. C. Yuan, B. B. Wang, Z. J. Robust, M.-R. Fire-Safe, *Macromol.* **2018**, *51*, 8001.
[36] A. Rekondo, R. Martin, A. R. D. Luzuriaga, G. Cabañero, H. J. Grandea, *Mater. Horiz.* **2014**, *1*, 237.
[37] S.-M. Kim, H. Jeon, S.-H. Shin, S.-A. Park, J. Jegal, S. Y. Hwang, D. X. Oh, J. Park, *Adv. Mater.* **2018**, *30*, 1705145.
[38] H. Yao, T. Liu, Y. Q. Jia, Y. J. Du, B. W. Yao, J. H. Xu, Fu, *Adv. Funct. Mater.* **2023**, *33*, 2307455.
[39] Y. Cao, H. P. Wu, S. I. Allec, B. M. Wong, D.-S. Nguyen, C. A. H. S. Wang, *Adv. Mater.* **2018**, *30*, 1804602.
[40] J. Kang, D. Son, G.-J. N. Wang, Y. X. Liu, J. Lopez, Y. Kim, J. Y. Oh, T. Katsumata, J. Mun, Y. Lee, L. H. Jin, J. B.-H. Tok, Z. N. Bao, *Adv. Mater.* **2018**, *30*, 1706846.
[41] R. B. Luo, H. B. Li, B. Du, S. S. Zhou, Y. X. A. Zhu, *Org. Electron.* **2020**, *76*, 105451.
[42] M. J. Liu, P. Liu, G. Lu, Z. T. Xu, X. A. Yao, *Chem. Int. Ed.* **2018**, *57*, 11242.
[43] R. B. Luo, X. Li, H. B. Li, B. Du, S. S. A. Zhou, *Prog. Org. Coat.* **2022**, *162*, 106593.
[44] C. J. Kloxin, In *Healable Polymer Systems*, (Eds.: W. Hayes, B. W. Greenland), The Royal Society of Chemistry, Cambridge, U.K. **2013**, pp. 62–91.
[45] S. Gong, Z. H. Zhu, J. Li, S. A. Meguid, *J. Appl. Phys.* **2014**, *116*, 194306.
[46] S. Ruth, V. Feig, H. Tran, Z. Bao, *Adv. Funct. Mater.* **2020**, *30*, 2003491.
[47] S. Lee, S.-H. Byun, C. Y. Kim, S. Cho, S. Park, J. Y. Sim, J.-W. Jeong, *Adv. Mater.* **2022**, *34*, 2204805.
[48] K. I. Kasozi, N. E. Mbiydzneyuy, S. Namubiru, A. A. Safiriyu, S. O. Sulaiman, A. O. Okpanachi, H. I. Ninsiima, *Afr Health Sci* **2018**, *18*, 828.
[49] T. Yu, X. Lü, Y. He, W. Bao, *Compos. Part B* **2025**, *307*, 112976.
[50] D. Yang, K. Zhao, R. Yang, S. Zhou, M. Chen, H. Tian, D. Qu, *Adv. Mater.* **2024**, *36*, 2403880.
[51] Y. Chen, M. Y. Gao, K. Chen, H. L. Sun, H. N. Xing, X. Q. Liu, W. J. Liu, H. Z. Guo, *Small* **2024**, *20*, 2400593.
[52] P. T. Sun, Z. Fang, W. Sima, C. L. Niu, T. Yuan, M. Yang, Q. C. Liu, W. X. Tang, *ACS Appl. Mater. Interfaces* **2024**, *16*, 60699.
[53] S. Kim, J. W. Kim, Y. H. Lee, Y. R. Jeong, K. Keum, D. S. Kim, H. C. Lee, J. S. Ha, *Chem. Eng. J.* **2023**, *464*, 142700.
[54] S. Xu, R. Li, S. Tian, J. Yu, C. An, K. Yang, J. Yang, L. Zhang, *Electron.* **2025**, *9*, 61.
[55] W. Miao, L. Laamari, J. Yu, S. Schreiber, L. Heer, J. Cui, J. Huang, H. Bai, *Adv. Sci.* **2025**, 08823.